The Astrophysical Journal, 945:54 (13pp), 2023 March 1 https://doi.org/10.3847/1538-4357/acb59b

UV and Hα HST Observations of Six GASP Jellyfish Galaxies

Marco Gullieuszik[1], Eric Giunchi[1,2], Bianca M. Poggianti[1], Alessia Moretti[1], Claudia Scarlata[3], Daniela Calzetti[4], Ariel Werle[1], Anita Zanella[1], Mario Radovich[1], Callum Bellhouse[1], Daniela Bettoni[1], Andrea Franchetto[1], Jacopo Fritz[5], Yara L. Jaffé[6], Sean L. McGee[7], Matilde Mingozzi[8], Alessandro Omizzolo[1,9], Stephanie Tonnesen[10], Marc Verheijen[11], and Benedetta Vulcani[1]

[1] INAF-Osservatorio astronomico di Padova, Vicolo Osservatorio 5, I-35122 Padova, Italy; marco.gullieuszik@inaf.it
[2] Dipartimento di Fisica e Astronomia, Università di Padova, Vicolo Osservatorio 3, I-35122 Padova, Italy
[3] Minnesota Institute for Astrophysics, School of Physics and Astronomy, University of Minnesota, 316 Church Street SE, Minneapolis, MN 55455, USA
[4] Department of Astronomy, University of Massachusetts, 710 N. Pleasant Street, LGRT 619J, Amherst, MA 01002, USA
[5] Instituto de Radioastronomia y Astrofisica, UNAM, Campus Morelia, AP 3-72, CP 58089, Mexico
[6] Instituto de Física y Astronomía, Universidad de Valparaíso, Avda. Gran Bretaña 1111, Valparaíso, Chile
[7] School of Physics and Astronomy, University of Birmingham, Birmingham B15 2TT, UK
[8] Space Telescope Science Institute, 3700 San Martin Drive, Baltimore, MD 21218, USA
[9] Specola Vaticana, 00120, Vatican City
[10] Center for Computational Astrophysics, Flatiron Institute, 162 5th Avenue, New York, NY 10010, USA
[11] Kapteyn Astronomical Institute, University of Groningen, Landleven 12, NL-9747 AV Groningen, The Netherlands
Received 2022 December 5; revised 2023 January 19; accepted 2023 January 19; published 2023 March 7

Abstract

Star-forming, Hα-emitting clumps are found embedded in the gaseous tails of galaxies undergoing intense ram pressure stripping in galaxy clusters, so-called jellyfish galaxies. These clumps offer a unique opportunity to study star formation under extreme conditions, in the absence of an underlying disk and embedded within the hot intracluster medium. Yet, a comprehensive, high-spatial-resolution study of these systems is missing. We obtained UVIS/Hubble Space Telescope (HST) data to observe the first statistical sample of clumps in the tails and disks of six jellyfish galaxies from the GASP survey; we used a combination of broadband (UV to I) filters and a narrowband Hα filter. HST observations are needed to study the sizes, stellar masses, and ages of the clumps and their clustering hierarchy. These observations will be used to study the clump scaling relations and the universality of the star formation process, and to verify whether a disk is irrelevant, as hinted at by results from jellyfish galaxies. This paper presents the observations, data reduction strategy, and some general results based on the preliminary data analysis. The high spatial resolution of UVIS gives an unprecedentedly sharp view of the complex structure of the inner regions of the galaxies and of the substructures in the galaxy disks. We found clear signatures of stripping in regions very close in projection to the galactic disk. The star-forming regions in the stripped tails are extremely bright and compact and we did not detect a significant number of star-forming clumps in regions where MUSE did not detect any. The paper finally presents the development plan for the project.

Unified Astronomy Thesaurus concepts: Galaxy evolution (594); Galaxy environments (2029); Ram pressure stripped tails (2126); Galaxy clusters (584); Galactic and extragalactic astronomy (563)

Supporting material: interactive figure

1. Introduction

Understanding the physical conditions that lead to the formation of new stars, and conversely to the halting of star formation activity, is central for astrophysics. Galaxy disks are the usual cradle for star formation (SF); this is a hierarchical process traced by star-forming regions, dubbed "clumps," which are ubiquitous in star-forming galaxies. High-z galaxies are dominated by bright clumps, which are larger and more massive than in the local universe (Elmegreen et al. 2007; Forster Schreiber et al. 2011; Guo et al. 2018; Zanella et al. 2019), although spatial resolution is clearly an important factor for the determination of clump properties, as shown by the analysis of lensed high-z galaxies (Cava et al. 2018; Meštrić et al. 2022). At low z, Hubble Space Telescope (HST) studies have been fundamental to obtaining a rich panorama of star-forming clumps in galaxy disks from a number of surveys such as, e.g., LARS (Messa et al. 2019), LEGUS (Calzetti et al. 2015), and DYNAMO (Fisher et al. 2017).

The SF activity is strongly influenced and can even be halted by a number of processes, some of which are directly related to the environment in which the galaxy resides. Ram pressure stripping (RPS; Gunn & Gott 1972), i.e., the removal of interstellar gas from the disk of star-forming galaxies due to the hydrodynamical interaction with the hot intergalactic medium, is one such process and it is believed to have a strong impact on galaxy populations in dense environments such as galaxy groups and, especially, clusters.

Our knowledge of the consequences of RPS for SF activity has greatly advanced in the last few years. It has been established that during the first phase of stripping, SF is enhanced in galaxy disks, both on kiloparsec scales and on galaxy-wide scales: most galaxies undergoing intense stripping lie above the relation between star formation rate (SFR) and stellar mass of normal galaxies (Vulcani et al. 2018; Boselli et al. 2023). The quenching sequence in stripped galaxies has

been directly observed, with outside-in quenching beginning in the external regions of the disk (Gullieuszik et al. 2017; Owers et al. 2019; Boselli et al. 2020) leading to Hα-truncated disks (Koopmann & Kenney 2004; Fritz et al. 2017) and then to post-starburst/post-SF disk galaxies (Vulcani et al. 2020a; Werle et al. 2022).

One of the most striking results about the RPS–SF connection is the discovery of large numbers of Hα-emitting clumps in the tails of stripped gas, up to 100–150 kpc away from the disk (Merluzzi et al. 2013; Fossati et al. 2016; Consolandi et al. 2017; Poggianti et al. 2019a). SF in stripped tails was seen by some hydrodynamical simulations, though they lack the capability to predict the characteristics of SF complexes (Kapferer et al. 2009; Tonnesen & Bryan 2012; Roediger et al. 2014; Lee et al. 2022). Observationally, Hα clumps, as well as interclump diffuse Hα emission, are common in the tails of so-called "jellyfish galaxies," whose long Hα tails are due to intense ram pressure in the central regions of galaxy clusters, where they move at high speed with respect to the intracluster medium (ICM) (Jaffé et al. 2018; Gullieuszik et al. 2020).

Recently, the study of jellyfish galaxies has moved from a few individual cases to statistical samples that have unveiled a number of results (Boselli et al. 2018; Moretti et al. 2018; Poggianti et al. 2019a, 2019b; Jáchym et al. 2019; Moretti et al. 2020a, 2020b). (a) The Hα emission of the clumps in the tails is mostly powered by stars formed in situ, without an underlying galaxy disk. (b) The diffuse emission in the tails is due to a combination of photoionization by young stars and heating (via shock heating or heat conduction), the latter most probably due to mixing of stripped gas with the hot ICM. (c) Following the discovery of large amounts of molecular gas in the stripped tails obtained with single-dish telescopes, molecular gas clumps have now been directly observed with the Atacama Large Millimeter/submillimeter Array (ALMA). (d) The properties of ∼500 Hα clumps in jellyfish tails have been studied at 1 kpc resolution, and associated stellar masses between 10^5 and 10^8 $M_\odot$ have been found (similar to high-z clumps). At these resolutions, the tail clumps seem to follow scaling relations (Hα luminosity versus gas velocity dispersion etc) similar to disk clumps.

The emerging picture is that gas stripped by ram pressure finds itself embedded in the hot intracluster plasma but manages to collapse and form new stars. The light of these young stars is directly observable in the UV (Smith et al. 2010; George et al. 2018, 2023). Depending on the galaxy, stars formed in the tails represent between a few percent and 20% of the total ongoing SFR of the system disk+tail (Poggianti et al. 2019a; Werle et al. 2022). Overall, tail clumps form stars at a higher rate than clumps in the disk with the same stellar mass density; however, if only the mass formed in the last 100 Myr is considered, the differences are reconciled, suggesting that the local mode of SF is similar in the disks and in the tails on timescales of 100 Myr (Vulcani et al. 2020b).

One crucial missing piece of the puzzle is a high-spatial-resolution study of star-forming clumps in the tails and disks of jellyfish galaxies. So far we have no handle on the sizes of a significant number of tail clumps, and cannot study all the other relevant quantities (stellar masses and ages, above all) on scales <1 kpc. Cramer et al. (2019) presented a subkiloparsec-scale study based on HST data of star-forming clumps in the D100 jellyfish tails; D100 is a low-mass galaxy in the Coma cluster that has yielded the size and age of three Hα-emitting tail clumps and sizes for seven other candidates. Another subkiloparsec-scale study presenting the properties—including the size—of star-forming clumps in RPS galaxies is the one presented by Boselli et al. (2021); that study, however, is focused on IC 3476, a low-mass galaxy in the Virgo cluster that hosts a very low SF activity in the tail, much lower than the typical SF of GASP galaxies (Gullieuszik et al. 2020).

In this paper we present HST observations of six spectacular jellyfish galaxies from the GASP survey (Poggianti et al. 2017). GASP has obtained MUSE@VLT integral field spectroscopy for 114 galaxies at $0.04 < z < 0.07$, including 94 ram pressure stripping candidates. Among these, a large number of jellyfish galaxies—defined as those with the stripped gas tail at least as long as the diameter of the galaxy's stellar disk—were found. GASP MUSE data are complemented by observing campaigns with JVLA, APEX and ALMA, MeerKAT, LOFAR, UVIT, and Chandra X-ray data to probe all the gas phases and galaxy components. GASP is providing a substantial contribution to our understanding of gas stripping processes and RPS in general; however, GASP results are hampered by the spatial resolution of the observations, which is, in the case of MUSE and ALMA data, ∼1″, which corresponds to ∼1 kpc at the redshift of GASP galaxies. As a consequence, GASP observations sample only the largest scales of the star-forming structures. The unique spatial resolution of HST overcomes this limitation and allows us to gather a fundamental piece of information for understanding RPS and SF processes in general. The observations presented in this paper probe the SF process under uniquely extreme conditions: in the tails, with no galaxy disk serving as cradle, surrounded by a hostile hot gaseous environment that in principle could disrupt star-forming complexes, heating them either by mixing, thermal conduction, or shocks. Here, there are self-standing regions that seem to suggest that the SF process—once initiated—cares little about its underlying and boundary conditions. These regions, however, have features that are uniquely found in RPS systems. Many star-forming regions in the stripped tails have elongated or head–tail structures known as fireballs (Kenney et al. 2014) with a spatial displacement of the UV and Hα emissions that probe SF at different timescales. Moreover young stellar clumps are often organized in long filaments. Both these features are observed in our galaxies and will be further discussed in Sections 4.2 and 4.4. Another relevant open question about star-forming regions in the RPS tails is whether, or at what scales, they are gravitationally bound or not; this has direct implications for the fate of these systems. Poggianti et al. (2019a) suggest that the stellar aggregates formed in the tails of stripped gas might contribute to the large population of globular clusters or dwarf galaxies observed in nearby galaxy clusters. Cramer et al. (2019), however, found that the star-forming clumps in D100 are not gravitationally bound and therefore their stars will be dispersed as a diffuse component of the intracluster light. Addressing this open question and determining the subsequent fate of the clumps requires high-spatial-resolution observations to reliably assess the size and mass of the clump; this is one of the key goals of our HST observations that will be addressed as a future development of the project.

In this paper we present: the HST observations (Section 2); the data reduction procedure and the evaluation of the data quality (Section 3); a discussion of some first qualitative results

Table 1
Target Galaxies

Galaxy (1)	Cluster (2)	R.A. (ICRS) (3)	Decl. (ICRS) (4)	$\log(M_\star/M_\odot)$ (5)	z (6)	z_{cl} (7)	Other Data (8)
JO175	A3716	20:51:17.578	−52:49:22.01	10.50	0.0467	0.0456	
JO201	A85	00:41:30.298	−09:15:45.90	10.79	0.0446	0.0557	a, b, d, i, j
JO204	A957	10:13:46.830	−00:54:51.14	10.61	0.0424	0.0450	a, b, e
JO206	IIZW108	21:13:47.402	+02:28:34.62	10.96	0.0511	0.0489	a, b, c, f, g
JW39	A1668	13:04:07.729	+19:12:38.36	11.23	0.0663	0.0634	f, k
JW100	A2626	23:36:25.045	+21:09:02.88	11.47	0.0619	0.0551	a, b, e, h, l

Note. Columns: name (1), host cluster (2), equatorial coordinates (3, 4), stellar mass (5), galaxy redshift (6), host cluster redshift (7), and other available data (8). Values are taken from Vulcani et al. (2018) and Gullieuszik et al. (2020). The other available data sets are: CO from APEX (a: Moretti et al. 2018); CO from ALMA (b: Moretti et al. 2020b); H I from JVLA (c: Ramatsoku et al. 2019; d: Ramatsoku et al. 2020; e: Deb et al. 2020); LOFAR 144 MHz continuum (f: Ignesti et al. 2022a); magnetic field from JVLA (g: Müller et al. 2021); X-ray from Chandra (h: Poggianti et al. 2019b, i: Campitiello et al. 2021); far-UV/near-UV from UVIT/ASTROSAT (j: George et al. 2018, k: George et al. 2023, l: Poggianti et al. 2019b).

Table 2
Description of the Observations

Filter (1)	Orbits (2)	N_{exp} (3)	Exp. Time (s) (4)	5σ Mag. Point Source (5)	5σ Mag. $1'' \times 1''$ (6)
F275W	2	4	5283	26.9	25.0
F336W	1	3	2512	26.8	24.9
F606W	0.5	3	1038	27.4	25.4
F814W	0.5	3	1058	26.5	24.5
F680N	1	3	2507	26.1	24.1

Note. Columns: filter name (1), number of orbits (2), number of subexposures (3), total exposure time—it is slightly different for each galaxy and here we report the mean value (4), 5σ magnitude limit representative for point sources, computed using 5×5 pixel regions (5), 5σ magnitude limit for $1'' \times 1''$ regions (6). The computation of the last two columns is described in Section 3.3.

(Section 4); the conclusions and a discussion of the development plan of this project and forthcoming papers (Section 5).

In this paper we adopt the standard concordance cosmology: $H_0 = 70$ km s^{-1} Mpc^{-1}, $\Omega_M = 0.3$, and $\Omega_\Lambda = 0.7$.

2. Observations

Observations were carried out with the UVIS channel of the WFC3 camera on board HST between 2020 October and 2021 April (GO-16223; PI Gullieuszik). All the HST data used in this paper can be found in MAST: 10.17909/tms2-9250.

Target galaxies were selected from the sample of GASP ram pressure stripping galaxies (Poggianti et al. 2017) with long Hα-emitting tails. The selection was based on the number of Hα clumps in the tails detected with MUSE (Poggianti et al. 2019a). The main properties of the six target galaxies are reported in Table 1. The papers published so far using available multi-wavelength observations are listed in the last column; more data (e.g., with MeerKAT, LOFAR, ATCA, and Chandra) are available and will be published in forthcoming papers.

To probe SF in both the tail and the disk we used the broadband filters F275W and F336W and the narrowband F680N, which includes the Hα spectral line at the redshift of the target galaxy. To subtract the continuum stellar emission from F680N and to probe the light in the visible band we also used the broadband filters F606W and F814W. We obtained five HST orbits[12] for each of the six target galaxies (two orbits in F275W, one each in F336W and F680N, and 0.5 orbit each in F606W and F814W) for a total of 30 orbits. For all observations we used a linear dither pattern to cover the gap between the two UVIS chips, and split the exposure time into four single exposures for F275W and three exposures for all the other four filters. Details are given in Table 2.

Following the latest recommendations from STScI (Instrument Science Report WFC3 2020-08), we used post-flash to mitigate the effects of UVIS Charge Transfer Efficiency (CTE) degradation. By using the calculations made with the Astronomer's Proposal Tool (APT) the post-flash was set to bring the average background level to 20 e^- per pixel to ensure that CTE losses remain at a manageable level.

3. Data Analysis

3.1. Data Reduction and Calibration

We retrieved from the STScI archive the FLC files with the calibrated images (including the CTE correction) for each of the subexposures. All files were reduced and calibrated with the CALWF3 code v3.6.0, including the 2.0 version of the CTE algorithm, which was released in 2021 April.

While individual FLC images taken with the same filters are perfectly astrometrically aligned, in most cases there are small misalignments between images taken with different filters. This is most likely due to the low number of stars bright enough in all filters. To tweak the astrometric solution, first of all we combined all subexposures taken with each filter; we took the F606W as an astrometric reference and selected, for each of the other five combined images, a number of astrometric reference sources in common with the F606W one, preferentially unsaturated stars, but also compact extragalactic sources. The target galaxies have long tails of gas with star-forming regions; these were not used as astrometric references because their emission can be displaced in observations at different wavelengths (see Section 4.4). In all cases we found a sufficient (>10) number of sources evenly distributed in the field of view. These were then used to align all combined images to the F606W one using the TWEAKREG task; the astrometric solution was then propagated back to the FLC files using TWEAKBACK.[13]

Cosmic-ray removal from HST data is a critical task. In our case it is particularly problematic for the narrowband F680N frames, as the exposure time is relatively long and we have

[12] An HST orbit is about 52 minutes long.

[13] TWEAKREG, TWEAKBACK, and ASTRODRIZZLE, which is used for the following step, are included in the DRIZZLEPAC Python package.

only three frames for each galaxy. Standard procedures could not provide a satisfactory result and we therefore adopted a slightly modified approach. The cosmic-ray maps for the F680N were computed by combining all the nine F606W, F680N, and F814W FLC frames that were taken during the same visit.

All FLC frames taken with each filter were then stacked together using AstroDrizzle. Following standard recommendations,[14] we resampled the stacked images with a pixel scale of 0.″04, and a PIXFRAC parameter set to 0.8 for the F275W images (for which we have four exposures) and to 1 for all the other filters (for which there are three exposures). The output images were visually inspected to look for residual cosmic rays. The inspection was done by comparing the images of each galaxy in the five filters; we flagged as cosmic rays compact, bright emitting regions detected in one filter only.

The final stacked images were then corrected for the Milky Way dust extinction using Schlafly & Finkbeiner (2011) reddening maps and the Cardelli et al. (1989) extinction curve.

The RGB images shown in Figure 1 are obtained using the F814W and F606W output images for the R and G channels, respectively; given the large difference in wavelength between the F814W/F606W and the F336W/F275W filters, for the B channel we created a pseudo B-band image as:

$$F_{\rm B} = 0.25(F_{\rm F275W} + F_{\rm F336W}) + 0.5\,F_{\rm F606W}. \quad (1)$$

We then performed a nonlocal means denoising on the three images used in the three channels using the scikit-image Python package[15] (van der Walt et al. 2014). All the images in the three channels have been normalized using lower and upper limits of 0 and 10^{-19} erg s^{-1} cm^{-2} Å^{-1} and an arcsinh stretching function. The six RGB images were scaled to have the same spatial scale in kpc/pixel in Figure 1.

3.2. Computing the Hα Flux

This subsection describes the procedure to evaluate the Hα emission flux from the F606W, F680N, and F814W observations. First, we assumed that the only line contributing to the F606W and F680N observed fluxes is Hα and that no line contributes to the F814W flux. Indeed other emission lines (Hβ and the [O III], [N II], and [S II] lines being the strongest) are in the spectral range covered by the three filters, but they have a minor contribution in most cases, as we will show in the following. This assumption can be written as

$$\begin{aligned} F_{\rm F606W} &= F^{\rm cont}_{\rm F606W} + F_{\rm H\alpha}/w_{\rm F606W} \\ F_{\rm F680N} &= F^{\rm cont}_{\rm F680N} + F_{\rm H\alpha}/w_{\rm F680N} \\ F_{\rm F814W} &= F^{\rm cont}_{\rm F814W} \end{aligned} \quad (2)$$

where $F_{\rm H\alpha}$ is the line flux (in erg s^{-1} cm^{-2}) and for each filter f:

1. F_f is the PHOTFLAM-calibrated average measured spectral flux density;
2. $F^{\rm cont}_f$ is the average spectral continuum flux density;
3. w_f is the effective filter width. This was calculated using the RECTWIDTH method from the STSDAS package SYNPHOT (STScI Development Team 2020).

We also assumed that the spectral continuum flux density is a linear function of the wavelength in the spectral region of F606W, F680N, and F814W:

$$\begin{aligned} F^{\rm cont}_{\rm F680N} &= a\,F^{\rm cont}_{\rm F606W} + b\,F^{\rm cont}_{\rm F814W} \\ a &= \frac{\lambda_{\rm F814W} - \lambda_{\rm F680N}}{\lambda_{\rm F814W} - \lambda_{\rm F606W}} \\ b &= \frac{\lambda_{\rm F680N} - \lambda_{\rm F606W}}{\lambda_{\rm F814W} - \lambda_{\rm F606W}}. \end{aligned} \quad (3)$$

λ_f values have been calculated by creating a flat spectrum in F_λ and using the SYNPHOT EFFECTIVE_WAVELENGTH method. The resulting equation is

$$F_{\rm H\alpha} = 411.6\,F_{\rm F680N} - 242.3\,F_{\rm F606W} - 169.4\,F_{\rm F814W}. \quad (4)$$

As mentioned at the beginning of this subsection, the procedure we adopted assumes the presence of no other lines except for Hα. In the following we quantitatively assess the systematic effects due to the presence of other emission lines in star-forming regions.

At the redshift of the target galaxies the [N II]6548 and [N II] 6583 lines are included in the spectral range of both the F606W and the F680N filters. Since the two lines are very close to Hα, their contribution is simply summed up to the contribution of Hα. Therefore Equation (4) actually provides the sum of the flux of Hα and of the [N II] lines. We calculated the ratio $Q_{\rm NII}$ between the flux of Hα and the total flux of the three lines for different values of [N II]6583/Hα assuming a fixed line ratio [N II]6583/[N II]6548 = 3.071 (Storey & Zeippen 2000). $Q_{\rm NII}$ is equivalent to the ratio between the actual value of the Hα flux and the value obtained from Equation (4). Results are shown in Figure 2. For star-forming regions ($\log$([N II]6583/Hα) $\lesssim -0.3$, red symbols) $Q_{\rm NII}$ is always larger than 0.6, which means that estimating the Hα flux using Equation (4) would overestimate the true flux by less than a factor ∼1.6. Even for the regions with the most extreme active galactic nucleus (AGN)- or LINER-like line ratios the real Hα flux is at least ∼40%–50% of the estimated value.

Evaluating the effects of Hβ and [O III] is less straightforward. At the redshift of the target galaxies these lines are in the F606W band and therefore their emission flux contributes to overestimating the F606W stellar continuum and consequently also the computed continuum in F680N (see Equation (3)); this results in a systematic underestimation of the Hα flux computed from Equation (4). To quantify this effect, we used synthetic spectra with different line ratios to compute the fluxes in the UVIS photometric band and then we compared the results of Equation (4) with the value of the input Hα flux. Both the creation of input spectra and the computation of synthetic photometry were carried out with SYNPHOT. For the model spectra a continuum described by a linear function of the wavelength was adopted; we made quantitative tests to verify that the shape of the continuum has negligible effects on the results. The emission lines of Hβ, Hα, and the [O III] doublet at 4959 and 5007 Å were modeled using Gaussian profiles.[16] We adopted fixed line ratios of 3.013 for [O III]5007/[O III]4959 (Storey & Zeippen 2000) and 2.86 for Hα/Hβ and created a series of synthetic spectra for different values of the [O III] 5007/Hα ratio. We then used SYNPHOT to compute the fluxes in the UVIS photometric bands, which were then used to evaluate $F_{\rm H\alpha}$ from Equation (4); the ratio between the input Hα flux and the resulting value is reported as $Q_{\rm OIII}$ in Figure 2.

[14] https://www.stsci.edu/scientific-community/software/drizzlepac.html
[15] https://scikit-image.org/

[16] The actual shape of the line profile is negligible for this analysis, as it is based on synthetic photometry on bands much wider than the line profiles.

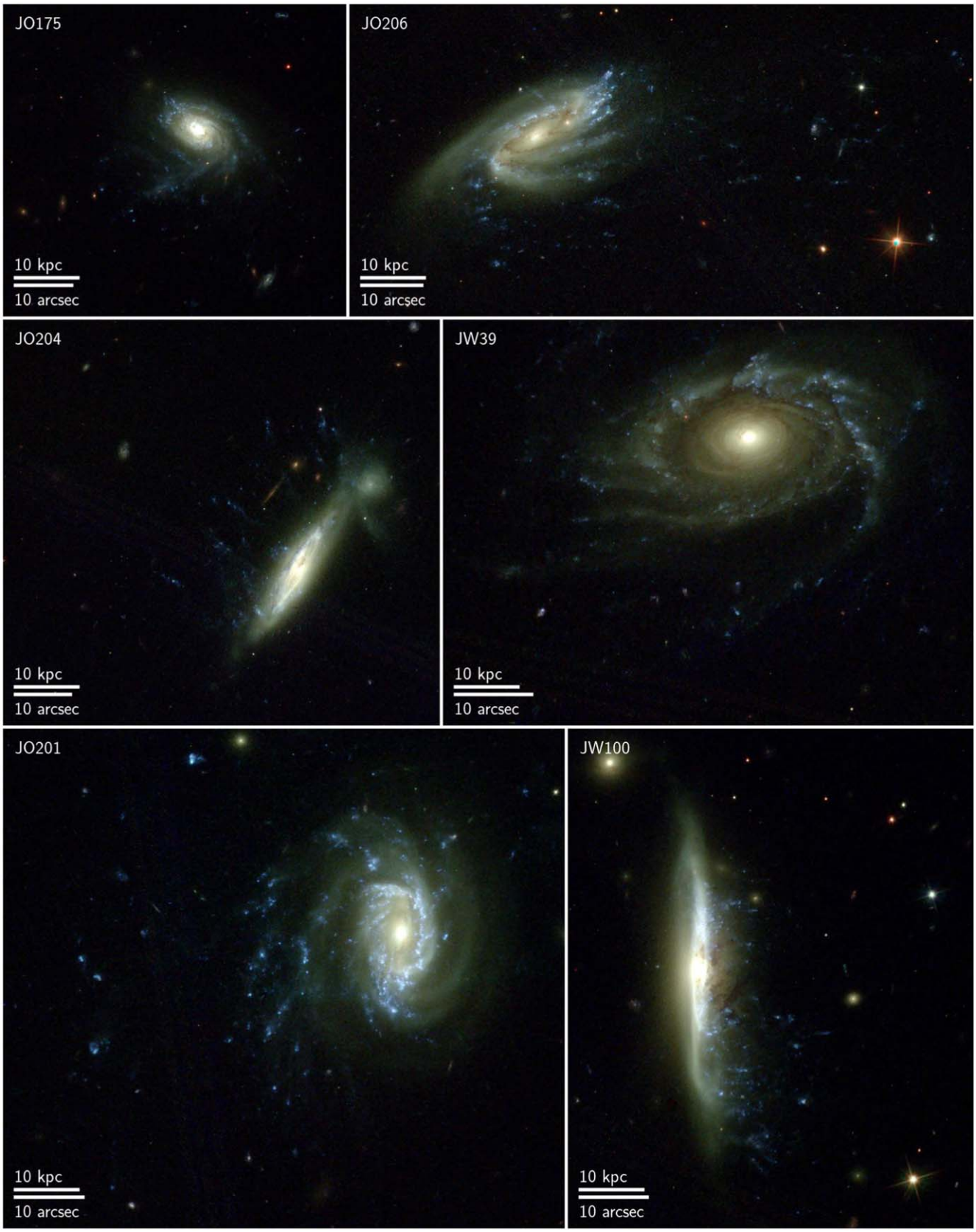

Figure 1. HST WFC3 images of the six observed galaxies (a description of the data used in each of the RGB channels is given at the end of Section 3.1). The scale in linear (kpc) and angular (arcsec) units is shown in the lower left corner of each panel. All images have been zoomed to have the same scale in linear units (kpc/pixel). The luminosity cuts and stretching function are the same for all galaxies. North is up and east is left.

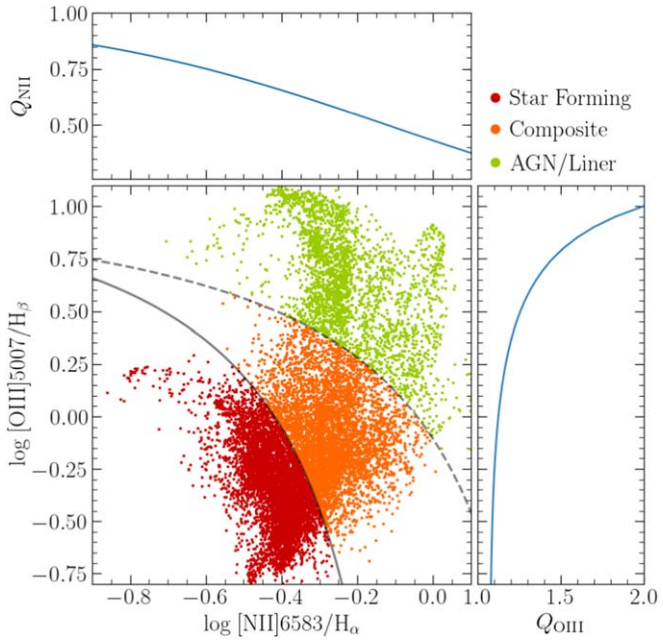

Figure 2. The effect of [O III] and Hβ lines on the Hα flux estimated from our HST data is shown in the right panel; the effect of the two [N II] lines in the top one (see text for details). The largest panel shows the range of [O III]/Hβ and [N II]/Hα line ratios using as a reference the Baldwin–Phillips–Terlevich (BPT) diagram obtained from MUSE observations of JO204 (Gullieuszik et al. 2017).

As expected, the Hα flux is always underestimated ($Q_{\rm OIII} > 1$); when the [O III] emission is weak the effect is dominated by the Hβ emission and it is ∼5%, which is negligible considering all the sources of uncertainty. In general, for star-forming regions ($\log([{\rm O\,III}]5007/{\rm H}\beta) \lesssim 0.25$, see central panel in Figure 2) $Q_{\rm OIII}$ is smaller than 1.2, which means that Hα is never underestimated by more than ∼15%.

The throughput of the F680N filter is essentially constant between 6800 and 7000 Å with variations of a few percent; at 7040 Å its value is decreased by 10% and at redder wavelengths it drops rapidly. This might be an issue only for JW39, which is the galaxy at the highest redshift (see Table 1); using results from GASP observations with MUSE we can safely assume that there should not be any Hα or [N II] emission at wavelengths longer than 7040 Å. We therefore conclude that the dependence of the filter throughput on wavelength has no significant effects on the Hα flux estimate.

We finally note that our considerations do not take into account the effects of dust. As dust attenuates Hβ and [O III] more than Hα emission it would therefore decrease the $Q_{\rm OIII}$ value; as a consequence, the values discussed above are upper limits because any SF regions would have non-negligible dust extinction.

We can therefore conclude that the main source of uncertainty in our method to derive the Hα flux is due to the contribution of the [N II] lines. All other emission lines play a second-order role that would in any case act in the opposite direction to that of [N II]; their contribution would therefore reduce the systematic effect due to the [N II] lines.

3.3. Background Variation, Noise, and Detection Limit

This subsection presents a statistical analysis of our images and assessment of the noise level and the magnitude limit of our observations.

By construction, the average background in the final images is zero, but small-amplitude residuals are present on large spatial scales. These are shown in Figure 3 for two galaxies as an example. With the aim of enhancing large-scale structures and minimizing the local noise, in Figure 3 we binned 10×10 the DRC images and the results were divided by 100; the values in the resulting image can therefore be interpreted as a spatially averaged image with the same intensity scale as the original image. We then smoothed the image by convolving it with a 2D Gaussian kernel with a standard deviation of 3 pixels. The rightmost panels in Figure 3 show also results for the Hα emission maps obtained as described in Section 3.2.

First of all we note that in some of the images there are discontinuities corresponding to the edges of the two UVIS chips and of the two readout amplifiers in each of them. Besides these, all other large-scale patterns are different from one image to the next; they might be due to a combination of uncertainties in the image reduction and calibration and/or to stray light components. We note that background variations are in all cases very small, of the order of 10^{-21} and 10^{-22} erg s^{-1} cm^{-2} Å^{-1} for the images in the two UV and the three visible filters, respectively. As we will show in the following, this is smaller than the average value of the local 1σ noise in the images. A further characterization of the background variations and an investigation of its origin are therefore beyond the scope of this paper because they do not significantly affect any of the conclusions of this work nor of the photometric measurements that will be used in follow-up analyses.

The drizzling procedure induces correlated noise (Gonzaga et al. 2012), which was evaluated by carrying out a statistical analysis on regions of different size, from 1 pixel (40 mas) to 25 pixels (1″). First of all, we selected for each galaxy 12 regions of 300×300 pixels with no bright sources (see Figure 3). Since some faint—not detected—sources might be present, for each region the background mean brightness value m and the rms noise σ were estimated with an iterative procedure. First guess values were estimated as the mean and the standard deviation of the counts in the region. We then fitted a Gaussian function to the values lower than $m + \sigma$. The m and σ values derived by the fitting procedure were then used to update the selection procedure, and the fitting procedure was repeated to obtain a final value for the mean and rms noise of the counts. We then rebinned each of the 12 cutout images (one for each of the 12 regions) using binning factors from 2 to 25, to estimate the statistical properties of the images on scales up to 1″ (25 pixels).

The standard deviation of the count rate in each of the 12 regions for all rebinning factors gives the noise on the corresponding spatial scale. The 12 noise values are consistent with each other, indicating, as expected, that the noise level of the background is substantially constant across the images. For each spatial scale we calculated the average and the standard deviation of the noise values obtained for each of the 12 regions; these are shown in Figure 4 as a blue shaded area. The figure also shows predictions for the correlated noise using the formula from Casertano et al. (2000); for images drizzled with a PIXFRAC parameter equal to p, the noise on scales corresponding to N pixels is

$$\overline{\sigma} = \sigma(1)/(1 - p/3)$$
$$\sigma(N) = \overline{\sigma}\, N(1 - p\, N/3). \quad (5F)$$

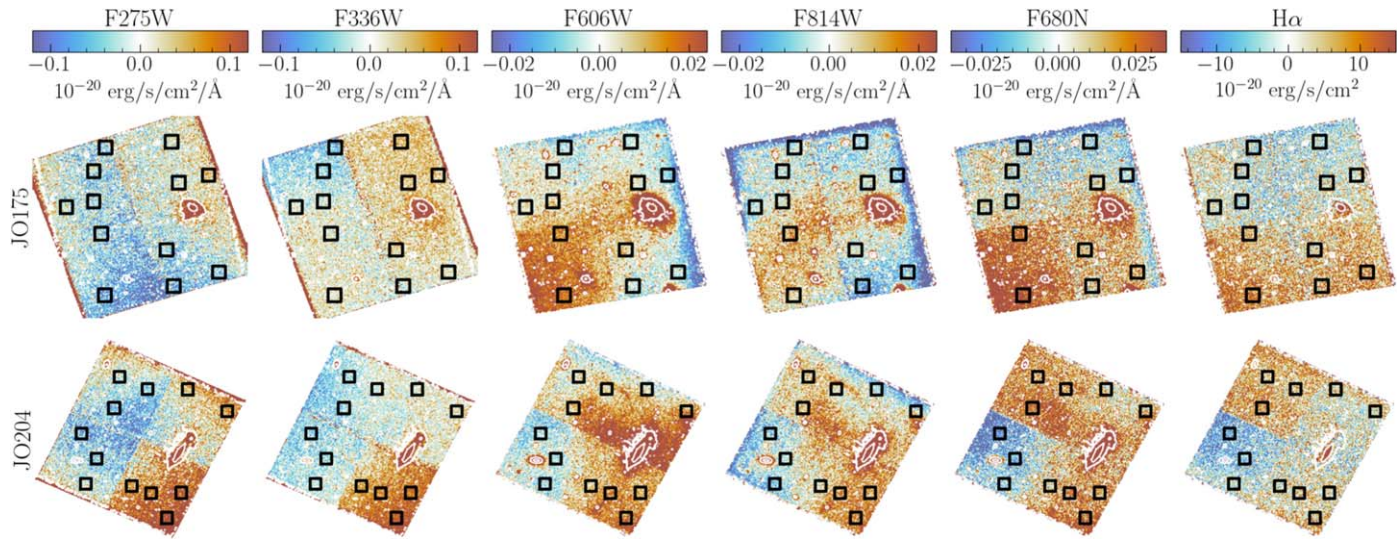

Figure 3. Images in the five UVIS filters and the Hα emission map for two target galaxies. Images were smoothed and convolved with a Gaussian kernel to reduce the noise on small spatial scales and to highlight large-scale background variations. The white contours are isophotes from the F606W image shown to visualize the stellar sources as a reference. The black squares show the 12 regions that were used to evaluate the statistical properties of the images.

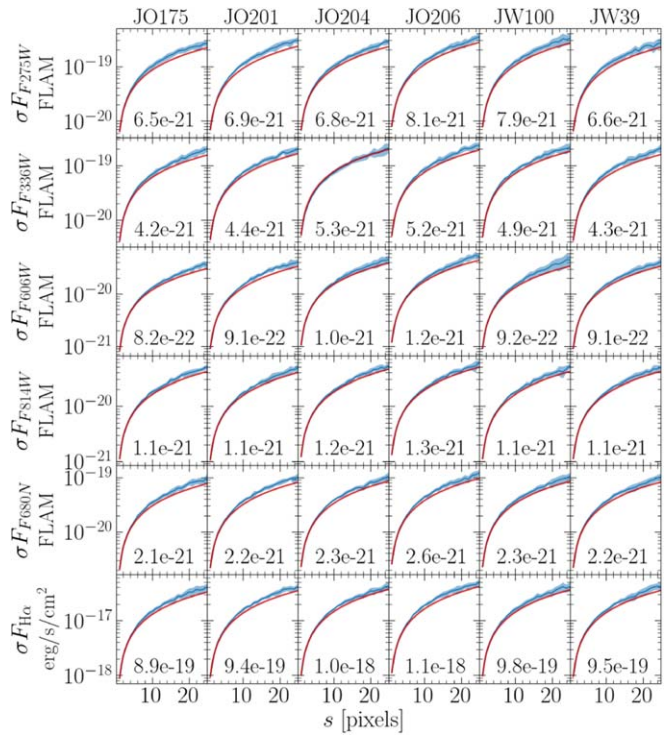

Figure 4. Mean value and dispersion (blue area) of the noise level at different scales computed in 12 different regions on each image. The red lines are predictions using the formula in Casertano et al. (2000). The values of the noise on 1 pixel scales σ_1 are reported in each panel. Noise values are in erg s^{-1} cm^{-2} Å^{-1} for the images in the five filters (panels in the top five rows) and in erg s^{-1} cm^{-2} for the Hα emission map (bottom row).

For our images $p = 0.8$ for F275W observations and 1.0 for all other filters (Section 3.1). These relations are shown as a red line in Figure 4 and show good agreement with our data; the noise model from Casertano et al. (2000) underestimates the observed values, particularly at large spatial scales. This is a well known fact that is commonly associated with a combination of the presence of very faint sources and small irregularities in the background, as was already found by Casertano et al. (2000).

These results were used to compute the magnitude limit of our observations. For each filter, we computed the mean values of the noise levels in Figure 4 and we converted them into AB magnitudes using the UVIS zero-points; to estimate the magnitude limit for detection of point sources we used the noise computed on 5×5 pixel regions, corresponding to the values generally used in the exposure time calculator; a magnitude limit more representative for extended sources was computed from the values obtained for $1'' \times 1''$. The results are shown in Table 2; they are in good agreement with the values obtained with the UVIS exposure time calculator. For the Hα flux we obtained 1σ detection limits of 7×10^{-18} erg s^{-1} cm^{-2} for point sources and 4×10^{-17} erg s^{-1} cm^{-2} arcsec^{-2} for diffuse emission.

At the redshift of the target galaxies ($z \sim 0.05$) the Hα detection limit for point sources corresponds to a luminosity $L_{\rm H\alpha} = 4 \times 10^{37}$ erg s^{-1}. This value is very similar to the luminosity of the faintest clumps detected for GASP galaxies with MUSE (Poggianti et al. 2019a). We note, however, that for clumps larger than the UVIS resolution (∼70pc FWHM) the star-forming clumps cannot be approximated by pointlike sources; in this case their flux would be spread over a larger area and consequently the detection limit would be brighter than the one estimated for pointlike sources.

4. Discussion

The spatial resolution of HST observations gives an unprecedentedly detailed view of the target galaxies; previous observations of these galaxies at visible wavelengths with VLT/MUSE (Poggianti et al. 2017) and in the UV with ASTROSAT/UVIT (George et al. 2018) have spatial resolution of the order of 1″; HST UVIS data are at least 10 times better than this, opening a completely new window to probe subkiloparsec-scale structures in GASP galaxies.

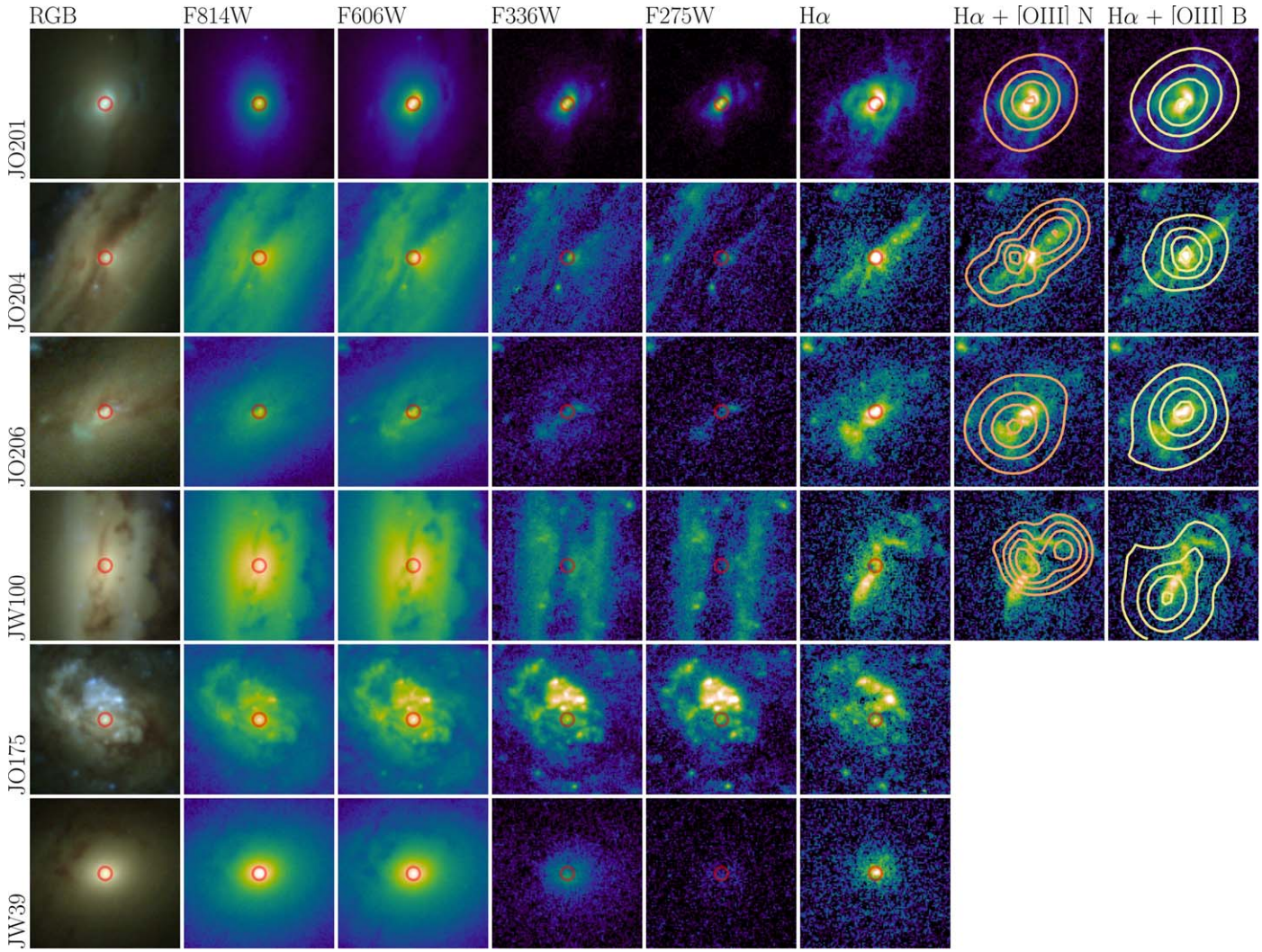

Figure 5. RGB image, Hα emission map, and broadband images of the central 4″ × 4″ of the six target galaxies. The red circle marks the center of each galaxy. The RGB images in the leftmost column are obtained in the same way as the other ones presented in this paper but using different luminosity cuts to better visualize the bright central regions. The background image in the two rightmost panels is the Hα emission map; the contours show the flux of the broad (light yellow) and narrow (light orange) components of the [O III]5007 line detected with MUSE (Radovich et al. 2019). An interactive visualization of the data presented here is available at https://web.oapd.inaf.it/gullieuszik/hst_gasp_centers and in the online journal.

4.1. Central Regions of the Galaxies

This subsection focus on the central region of the six target galaxies; the UVIS data allow us to study with unprecedentedly high resolution the source of the bright central emission and to complement the available MUSE spectroscopy to better constrain its nature. Results from the GASP survey showed that JO201, JO204, JO206, and JW100 galaxies host an AGN (Radovich et al. 2019); the central region of JW39 has a LINER-like spectrum (Peluso et al. 2022); finally ionization in the central region of JO175 is dominated by SF activity (Poggianti et al. 2019a; Radovich et al. 2019).

The central regions of the galaxies are shown in Figure 5. A large number of very compact sources are detected in the central region of JO175; they are bright both in the UV and in the Hα maps and faint in F814W; we can therefore conclude they are young star-forming regions, confirming the results obtained from MUSE (Poggianti et al. 2019a; Radovich et al. 2019). JW39 emission is dominated by a source with a regular elliptical morphology at the center of the galaxy; it is clearly detected in Hα and in F336W but is extremely faint in F275W; indeed among the six central sources it is the one with the reddest F275W – F336W color; the most plausible scenario is that the central region is obscured by dust and older than the central regions of the other galaxies.

All the other four galaxies host an AGN; the [O III]5007 line is therefore expected to be extremely strong in the central regions and therefore the Hα flux we computed could be significantly underestimated as discussed in Section 3.2; we note that none of the conclusions of this paper, nor any planned analysis, will be based on the Hα flux of the regions dominated by AGNs.

The morphology of the central regions for these galaxies varies significantly at the different wavelengths (Figure 5). Multiple dust lanes are present in the nuclear regions, in particular in JO204, JO206, and JW100: this is often observed in HST images of type-2 AGNs (see, e.g., Keel et al. 2015; Ma et al. 2021). In particular, Keel et al. (2015) attributed the presence of irregularly distributed dust lanes, similar to those observed here, to ongoing or past interaction processes.

HST observations also reveal the detailed morphology of the bright Hα emission already observed with MUSE, which was

proved to be predominantly ionized by the AGN based on the analysis of the emission line ratios in MUSE (Radovich et al. 2019). MUSE data also showed that emission lines in JO201, JO204, and JW100 clearly present at least two components in the line profiles, one *broader* ($\sigma_v \sim 200$–500 km s^{-1}) and the other *narrower* ($\sigma_v < 200$ km s^{-1}). Both components can be related to outflows, which in Radovich et al. (2019) were defined as those cases where the line velocities deviate significantly from the rotational field traced by stellar velocities measured at the same positions (see also, e.g., Davies et al. 2020). In Figure 5 we overlay on the HST Hα images the contour maps of the [O III]5007 flux in these two components. This allows us to compare the HST Hα properties with the analysis of outflow properties done in Radovich et al. (2019), to which we refer for more details. In JO201 both [O III] components overlap well with the Hα central, more compact emission; this agrees with the interpretation that in JO201 the outflow orientation is close to the line of sight. In JO204 the Hα emission shows a more extended structure: the broader [O III] component overlaps with the central emission, and the narrower one is peaked at two opposite positions along the Hα emission; both components were associated with the outflow. Similarly, in JW100 there are two [O III] components of similar width ($\sigma_v < 200$ km s^{-1}) emitted by distinct regions along the Hα emission and merging into a double-peaked profile in the inner regions, which were also associated with an outflow. Finally, [O III] shows a very faint broader component in the central MUSE spaxels of JO206, and Radovich et al. (2019) concluded that it was not possible to detect a meaningful outflow component: we notice, however, that this component overlaps well with the Hα peak. The dominant, narrower component still follows the Hα emission, but there is an offset between the peaks of the two maps. To summarize, though both the broader and narrower components may be related to outflows and the Hα maps include the contribution from both, it can be seen that the emission from the broader component is peaked on the central Hα emission, thus confirming that it is mostly emitted by the inner nuclear regions. The narrower components are instead coincident with a more extended Hα emission.

4.2. Galaxy Disk and Stripped Gas in the Inner Regions

The high potential of the diagnostic power of UVIS observations can be appreciated in Figure 6, in which we show a zoom on the galaxy disks of JO204, JO206, and JW100 of the RGB images from Figure 1. The same figure also shows the F275W and F814W images, to probe star-forming and intermediate–old stellar populations. In each panel we also show, as a reference, the line derived from GASP data to define the stellar disk and the stripped gas tail (Gullieuszik et al.2020).

HST observations provide a much more detailed view of the complex structure of the galaxy disk and of the inner galactic regions. The 1 kpc spatial resolution of MUSE and UVIT observations does not allow us to clearly resolve and characterize substructures, in particular for galaxies with a substantial inclination in the plane of the sky. As a consequence, it is also extremely difficult to clearly disentangle structures belonging to the disk and to the stripped tail; previous GASP works therefore adopted a conservative approach to define SF regions that can be safely classified as being formed in the stripped gas tail. This was done by considering the stellar continuum emission and using the isophote corresponding to a surface brightness 1σ above the average background. The isophote is not symmetric due to RPS and hence an ellipse was fitted to the undisturbed side of the isophote; this ellipse was used to replace the isophote on the disturbed side (for details see Gullieuszik et al. 2020). The resulting contour line is shown in green in Figure 6. HST observations allow us to go beyond this simple approach and they provide robust clues to how RPS affects the inner region of galaxies. Figure 6 shows bright regions in the disk that are particularly bright in the UV and barely visible—or not visible at all—in the F814W image; they hence stands out as bright and blue sources in the RGB images. Most of them have also Hα emission associated with the UV-bright emission. We also note that they are organized in filamentary structures aligned in the direction of the tail. For these reasons we can safely conclude that the observed bright regions are young stellar clumps that are formed in gas stripped from the stellar disk by ram pressure. Being so close to the galactic disk, we cannot say whether they are still gravitationally bound to the galaxy—and will eventually fall back into the galaxy disk—or not—and hence will be completely stripped and lost in the ICM. A further investigation and characterization of these regions in the disk that are affected by gas stripping is presented in Giunchi et al. (2023).

Many SF regions are organized in filamentary structures, in agreement with cloud-crushing simulations of cold clouds in a hot wind; these have been able to produce long tails of cold, dense gas that are about as wide as the cloud and extend for tens of cloud radii when the radiative cooling time is shorter than the cloud destruction time (e.g., Gronke & Oh 2018; Abruzzo et al. 2022; Tan et al. 2023). Recent simulations have found star formation within these streams from individual dense $\sim$100 pc clouds (S. Tonnesen & R. Smith 2023, in preparation).

4.3. Star-forming Clumps and Diffuse Emission

A major point that previous GASP observations could not address directly concerns the nature of the diffuse Hα emission observed in GASP galaxies (Tomičić et al. 2021a, 2021b, and references therein); in the tail, the diffuse emission (defined as the Hα component outside compact clumps) is found to be 50% on average and up to 80% in some galaxies (Poggianti et al. 2019a). Diagnostic BPT diagrams based on the [N II]/Hα line ratio indicate that the dominant ionization source of the diffuse emission is SF. However, MUSE data show that other mechanisms are at play, such as mixing, shocks, and accretion of intercluster and interstellar medium gas (Tomičić et al. 2021a, 2021b). MUSE observations could not firmly establish whether the diffuse emission powered by SF was due to ionizing radiation escaped from the star-forming clumps detected by MUSE or from a population of smaller and undetected star-forming clumps that are hiding within the diffuse Hα emission in the tails.

In Giunchi et al. (2023) we present a thorough characterization of the star-forming clumps detected from the UVIS observations presented in this paper. These are identified in either UV or Hα with luminosity down to $\sim 10^{36}$ erg s^{-1} Å^{-1} in F275W and $\sim 10^{38}$ erg s^{-1} in Hα; these values are very close to the detection limit computed in Section 3.3. We did not detect any significant population of compact sources in UV or Hα in the tails outside of the star-forming clumps detected with MUSE (see Poggianti et al. 2019a). Hence we can safely

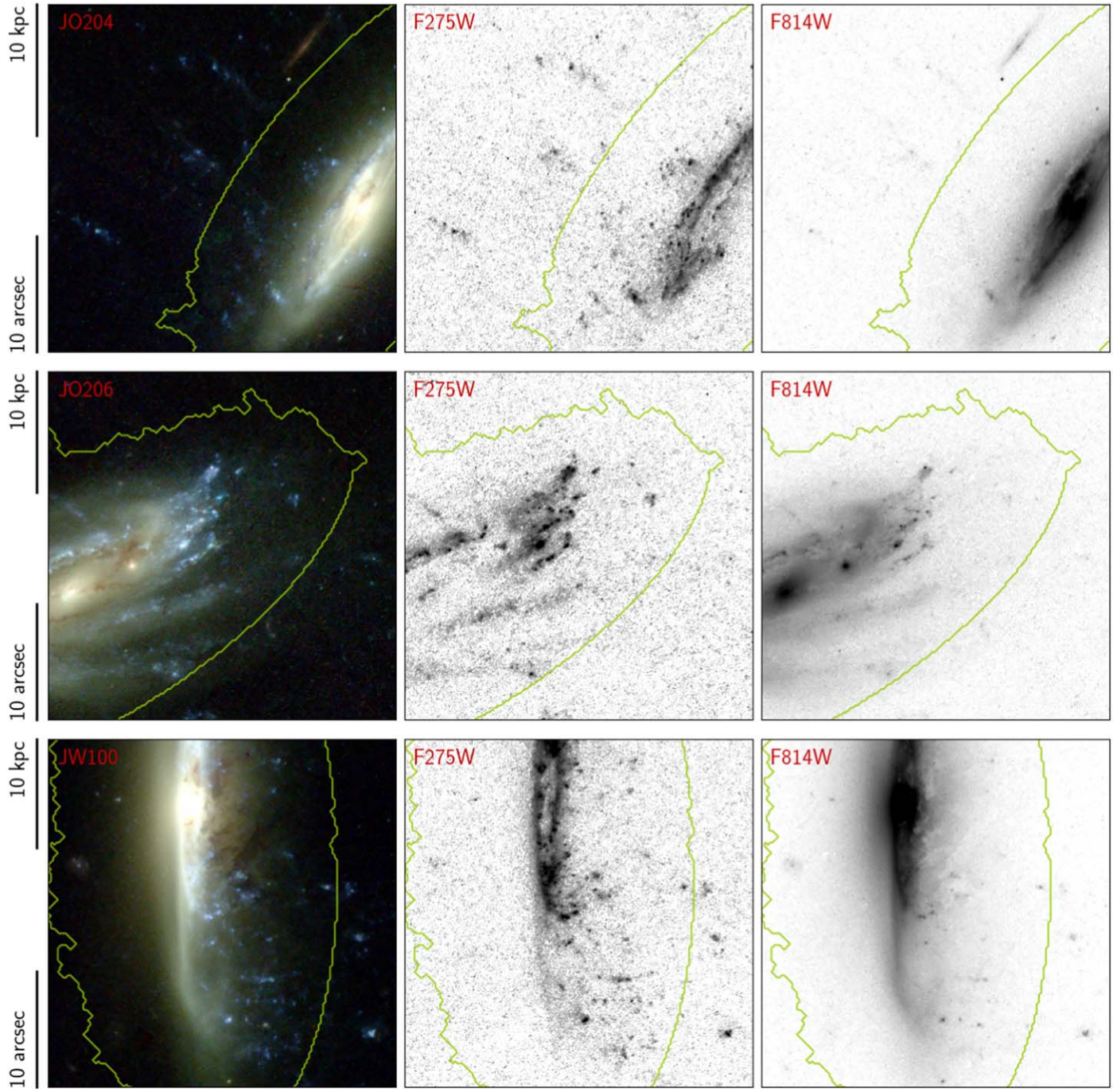

Figure 6. RGB, F275W, and F814W images of JO204, JO206, and JW100. The green line is the galaxy disk contour derived from MUSE observations (Gullieuszik et al. 2020).

conclude that the ionizing source of what was defined as diffuse ionized emission from MUSE data is not in situ SF in clumps brighter than the detection limit of our HST observations.

Another interesting result from Giunchi et al. (2023) is that the sizes of the clumps in the tails measured from the HST observations are generally smaller than what was estimated in Poggianti et al. (2019a) from MUSE observations using the luminosity–size relation for H II regions from Wisnioski et al. (2012). However, we found that at a given size, tail clumps are ∼10 times brighter than the H II regions observed by Wisnioski et al. (2012). The paucity of very large star-forming clumps (larger than a few hundred parsecs) and/or the compactness of the star-forming clumps in the tails might be connected with the peculiar physical condition in the ram pressure-stripped gas, which might affect the SF process. In principle, the collapse of molecular clouds and the SF processes could be influenced by thermal conduction from the ICM; however, this effect could be mitigated or even prevented by magnetic fields (Müller et al.2021; Ignesti et al. 2022b). The complex interplay between the stripped gas and the ICM would also affect the turbulence of the gas in the tails and hence the properties of the clustering hierarchy, which should hence be linked to the environment and its pressure.

Future work based on the observations presented here and on the properties of the SF regions detected in Giunchi et al. (2023) will study the dependence of SF clustering on local environment by comparing the size distributions and fractal properties of the SF regions in the tails and in the disks with those of undisturbed galaxies.

4.4. UV and Hα

Since the gas in the tail is constantly accelerated by ram pressure it is expected that stellar populations of different ages formed by the same parent gas cloud might be found at slightly different spatial locations; RPS tails show fireball structures (see, e.g., Kenney et al. 2014) with elongated UV emission (tracing SF on timescales $\sim 10^8$ yr) that in some cases have head–tail structure and compact Hα emission (tracing SF on timescales $\sim 10^7$ yr) located on the head—in the direction of the ram pressure wind. Numerical simulations predict general alignment of Hα and UV emission, with UV emission extending somewhat closer to the disk and Hα emission extending slightly further from it. This partially differs from the ∼100 pc displacement between UV and Hα emission that was found, for example, in the tail of IC 3418 by Kenney et al. (2014). In our data there are some notable examples of this effect, and two of them are shown in Figure 7. The head–tail structures detected in the UV have sizes of a few hundred parsecs and the Hα emission is concentrated in compact regions on one side of the extended UV emission, in the downstream direction of the ram pressure wind; the peaks of Hα and UV emission, however, are coincident. This tends to be in better agreement with what is seen in simulations.

Galaxy-scale simulations generally do not reproduce clear stellar age gradients in the tail, although some of this can be blamed on their inability to resolve the displacements observed in our star-forming clumps (e.g., Kapferer et al. 2009; Tonnesen & Bryan 2012; Roediger et al. 2014). In the cloud-scale simulations of S. Tonnesen & R. Smith (2023, in preparation), age gradients are not universally seen in the stars formed in stripped clouds. They find that the faster and denser a wind is, the more likely it is that an age gradient is produced that would be reflected in an observed displacement of UV and Hα. In addition, more diffuse clouds that are still able to collapse are more likely to show age gradients.

A systematic quantitative analysis of the different morphologies of UV and Hα emission is beyond the scope of this paper. Ongoing and planned work on these observations includes a systematic search and characterization of SF regions and a detailed analysis of the stellar populations using spectral energy distribution (SED) fitting. Forthcoming papers based on the observations presented in this paper will therefore thoroughly examine the points briefly discussed in this section.

5. Summary and Project Development Plan

This paper presents UVIS HST observations of six RPS galaxies at redshift $z \sim 0.05$ from the GASP survey (Poggianti et al. 2017); they were selected for hosting a large number of star-forming clumps in the tails of stripped gas (see Poggianti et al. 2019a). Observations were carried out in four broad bands covering a spectral range from UV to the I band (F275W, F336W, F606W, and F814W) and one narrow band (F680N) covering Hα emission at the redshift of the target galaxies.

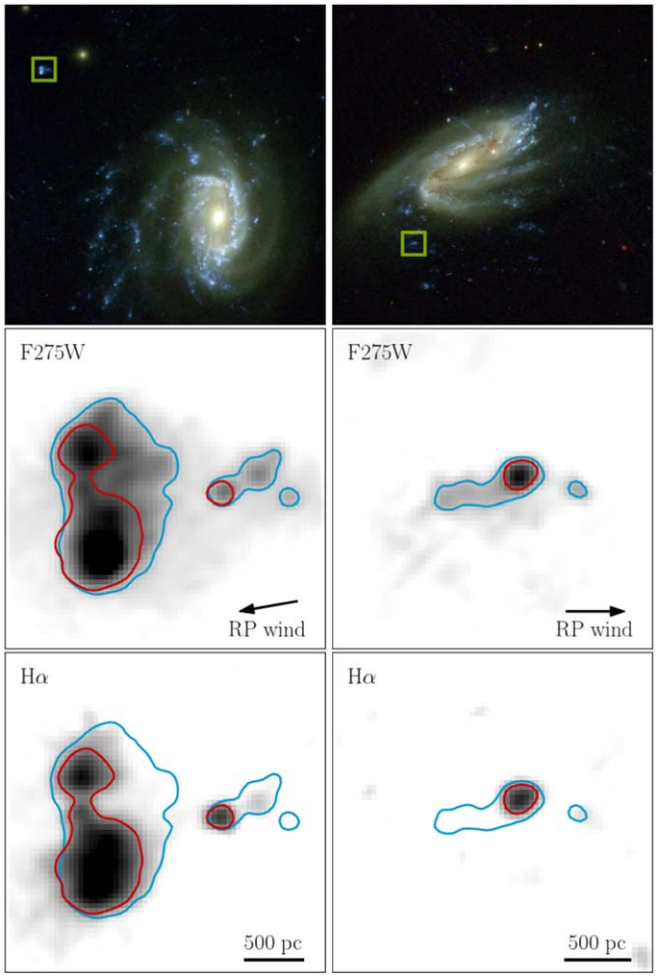

Figure 7. Zoom of the F275W and Hα images of JO201 (left panels) and JO206 (right panels) on two SF regions; their position is marked by the green squares in the top panels. The blue and red lines are isophotes of the F275W and Hα emission, respectively, which are overplotted to highlight the differences in the spatial distribution of Hα and UV emission. The arrows in the central panels suggest the approximate direction of the ram pressure wind.

The main goal of this observing program is to complement the large data set collected within the GASP project, which is based on MUSE observations and which was then followed-up with multiwavelength observations with JVLA, APEX and ALMA, MeerKAT, LOFAR, UVIT, and archival Chandra X-ray data to probe molecular and neutral gas, as well as UV and X-ray emission. The main limitation of these data is the spatial resolution, which is of the order of 1″ for all observations, corresponding to ∼1 kpc. The HST observations presented here allow studies of GASP galaxies with unprecedented spatial resolution; this is a critical aspect, in particular for characterizing SF regions that are in general small sources with subkiloparsec scales. Moreover, these observations provide deep UV data that would strongly constrain the properties of young stellar populations, as well as Hα data probing the ionized gas.

This paper presents a general description of the observations and the data reduction process; it also presents some general discussion and results that have been drawn from a preliminary analysis of the data. These can be briefly summarized as follows.

1. We do not detect a significant number of compact Hα or UV sources in Hα-emitting regions outside the star-forming clumps detected with MUSE. This shows that the ionizing source of this diffuse ionized gas component is not in situ SF in clumps above the UVIS detection limit ($L_{\rm H\alpha} = 10^{38}$ erg s^{-1} at 2σ).
2. The vast majority of the clumps detected in the stripped gas are not complex structures; HST images reveal that nearly all clumps detected with MUSE are single compact and bright sources.
3. Thanks to the extraordinary spatial resolution of HST we found clear signatures of stripping also in regions that are very close in projection to the galaxy disks.
4. There are some examples of tail clumps that show a clear difference in the UV and Hα emission. UV emission is elongated in the direction of the velocity of the galaxy in the ICM (and hence of the RPS) while Hα is concentrated on the side of the UV emission opposite to the position of the galaxy. This fireball structure (see Kenney et al. 2014) is the effect of the different ages probed by UV and Hα for a star-forming gas cloud that is accelerated by ram pressure.

The project based on the HST observations presented here will be developed in a series of research programmes. As already mentioned, a thorough analysis of the star-forming clumps is presented in Giunchi et al. (2023). With ongoing SED analysis of the star-forming clumps we are analyzing the properties of the stellar populations (ages, star formation histories, and stellar masses) of the star-forming regions in the stripped tails and in the galactic disk. The sizes and masses of individual clumps are crucial to establishing the current nature of the clumps, to investigating whether they resemble the properties of, e.g., globular clusters, ultracompact dwarfs, or dwarf spheroidals, and to understanding what their future evolution might be. To date, the limited spatial resolution of the available data could provide only upper limits on individual masses and most probably largely inflated sizes; these cannot provide sufficient constraints and are compatible with all the above-mentioned hypotheses (Poggianti et al. 2019a). HST data provide for the first time the accuracy required to reliably assess the nature and fate of the observed clumps.

We would like to sincerely thank the referee for their constructive comments that helped us to improve the quality of our manuscript. We warmly thank Jay Anderson, Crystal Mannfolk, and the HST Help Desk staff for the valuable support. This research is based on observations made with the NASA/ESA Hubble Space Telescope obtained from the Space Telescope Science Institute, which is operated by the Association of Universities for Research in Astronomy, Inc., under NASA contract NAS 526555. These observations are associated with program GO-16223. This research made use of Astropy, a community-developed core Python package for Astronomy (Astropy Collaboration, The Astropy Collaboration 2018). This project has received funding from the European Research Council (ERC) under the European Union's Horizon 2020 research and innovation program (grant agreement No. 833824). and "INAF main-streams" funding program (PI B. Vulcani). Y.J. acknowledges financial support from ANID BASAL Project No. FB210003.

Software: Python, astropy (The Astropy Collaboration 2018), synphot (STScI Development Team 2020).

ORCID iDs

Marco Gullieuszik https://orcid.org/0000-0002-7296-9780
Eric Giunchi https://orcid.org/0000-0002-3818-1746
Bianca M. Poggianti https://orcid.org/0000-0001-8751-8360
Alessia Moretti https://orcid.org/0000-0002-1688-482X
Claudia Scarlata https://orcid.org/0000-0002-9136-8876
Daniela Calzetti https://orcid.org/0000-0002-5189-8004
Ariel Werle https://orcid.org/0000-0002-4382-8081
Anita Zanella https://orcid.org/0000-0001-8600-7008
Mario Radovich https://orcid.org/0000-0002-3585-866X
Callum Bellhouse https://orcid.org/0000-0002-6179-8007
Daniela Bettoni https://orcid.org/0000-0002-4158-6496
Andrea Franchetto https://orcid.org/0000-0001-9575-331X
Jacopo Fritz https://orcid.org/0000-0002-7042-1965
Yara L. Jaffé https://orcid.org/0000-0003-2150-1130
Sean L. McGee https://orcid.org/0000-0003-3255-3139
Matilde Mingozzi https://orcid.org/0000-0003-2589-762X
Alessandro Omizzolo https://orcid.org/0000-0002-0838-6580
Stephanie Tonnesen https://orcid.org/0000-0002-8710-9206
Marc Verheijen https://orcid.org/0000-0001-9022-8081
Benedetta Vulcani https://orcid.org/0000-0003-0980-1499

References

Abruzzo, M. W., Bryan, G. L., & Fielding, D. B. 2022, ApJ, 925, 199
Boselli, A., Fossati, M., Ferrarese, L., et al. 2018, A&A, 614, A56
Boselli, A., Fossati, M., Longobardi, A., et al. 2020, A&A, 634, L1
Boselli, A., Fossati, M., Roediger, J., et al. 2023, A&A, 669, A73
Boselli, A., Lupi, A., Epinat, B., et al. 2021, A&A, 646, A139
Calzetti, D., Lee, J. C., Sabbi, E., et al. 2015, AJ, 149, 51
Campitiello, M. G., Ignesti, A., Gitti, M., et al. 2021, ApJ, 911, 144
Cardelli, J. A., Clayton, G. C., & Mathis, J. S. 1989, ApJ, 345, 245
Casertano, S., de Mello, D., Dickinson, M., et al. 2000, AJ, 120, 2747
Cava, A., Schaerer, D., Richard, J., et al. 2018, NatAs, 2, 76
Consolandi, G., Gavazzi, G., Fossati, M., et al. 2017, A&A, 606, A83
Cramer, W. J., Kenney, J. D. P., Sun, M., et al. 2019, ApJ, 870, 63
Davies, R., Baron, D., Shimizu, T., et al. 2020, MNRAS, 498, 4150
Deb, T., Verheijen, M. A. W., Gullieuszik, M., et al. 2020, MNRAS, 494, 5029
Elmegreen, D. M., Elmegreen, B. G., Ravindranath, S., & Coe, D. A. 2007, ApJ, 658, 763
Fisher, D. B., Glazebrook, K., Damjanov, I., et al. 2017, MNRAS, 464, 491
Forster Schreiber, N. M., Shapley, A. E., Genzel, R., et al. 2011, ApJ, 739, 45
Fossati, M., Fumagalli, M., Boselli, A., et al. 2016, MNRAS, 455, 2028
Fritz, J., Moretti, A., Gullieuszik, M., et al. 2017, ApJ, 848, 132
George, K., Poggianti, B. M., Gullieuszik, M., et al. 2018, MNRAS, 479, 4126
George, K., Poggianti, B. M., Tomicic, N., et al. 2023, MNRAS, 519, 2426
Giunchi, E., Gullieuszik, M., Poggianti, B., et al. 2023, ApJ, submitted (arXiv:2302.10615)
Gonzaga, S., Hack, W., Fruchter, A., & Mack, J. 2012, The DrizzlePac Handbook (Baltimore, MD: STScI)
Gronke, M., & Oh, S. P. 2018, MNRAS Lett., 480, L111
Gullieuszik, M., Poggianti, B. M., Moretti, A., et al. 2017, ApJ, 846, 27
Gullieuszik, M., Poggianti, B. M., McGee, S. L., et al. 2020, ApJ, 899, 13
Gunn, J. E., & Gott, J. R., III 1972, ApJ, 176, 1
Guo, Y., Rafelski, M., Bell, E. F., et al. 2018, ApJ, 853, 108
Ignesti, A., Vulcani, B., Poggianti, B. M., et al. 2022a, ApJ, 937, 58
Ignesti, A., Vulcani, B., Poggianti, B. M., et al. 2022b, ApJ, 924, 64
Jáchym, P., Kenney, J. D. P., Sun, M., et al. 2019, ApJ, 883, 145
Jaffé, Y. L., Poggianti, B. M., Moretti, A., et al. 2018, MNRAS, 476, 4753
Kapferer, W., Sluka, C., Schindler, S., Ferrari, C., & Ziegler, B. 2009, A&A, 499, 87
Keel, W. C., Maksym, W. P., Bennert, V. N., et al. 2015, AJ, 149, 155
Kenney, J. D. P., Geha, M., Jáchym, P., et al. 2014, ApJ, 780, 119
Koopmann, R. A., & Kenney, J. D. P. 2004, ApJ, 613, 866
Lee, J., Kimm, T., Blaizot, J., et al. 2022, ApJ, 928, 144
Ma, J., Maksym, W. P., Fabbiano, G., et al. 2021, ApJ, 908, 155
Merluzzi, P., Busarello, G., Dopita, M. A., et al. 2013, MNRAS, 429, 1747

Messa, M., Adamo, A., Östlin, G., et al. 2019, MNRAS, 487, 4238
Meštrić, U., Vanzella, E., Zanella, A., et al. 2022, MNRAS, 516, 3532
Moretti, A., Paladino, R., Poggianti, B. M., et al. 2018, MNRAS, 480, 2508
Moretti, A., Paladino, R., Poggianti, B. M., et al. 2020a, ApJ, 889, 9
Moretti, A., Paladino, R., Poggianti, B. M., et al. 2020b, ApJL, 897, L30
Müller, A., Poggianti, B. M., Pfrommer, C., et al. 2021, NatAs, 5, 159
Owers, M. S., Hudson, M. J., Oman, K. A., et al. 2019, ApJ, 873, 52
Peluso, G., Vulcani, B., Poggianti, B. M., et al. 2022, ApJ, 927, 130
Poggianti, B. M., Moretti, A., Gullieuszik, M., et al. 2017, ApJ, 844, 48
Poggianti, B. M., Gullieuszik, M., Tonnesen, S., et al. 2019a, MNRAS, 482, 4466
Poggianti, B. M., Ignesti, A., Gitti, M., et al. 2019b, ApJ, 887, 155
Radovich, M., Poggianti, B., Jaffé, Y. L., et al. 2019, MNRAS, 486, 486
Ramatsoku, M., Serra, P., Poggianti, B. M., et al. 2019, MNRAS, 487, 4580
Ramatsoku, M., Serra, P., Poggianti, B. M., et al. 2020, A&A, 640, A22
Roediger, E., Bruggen, M., Owers, M. S., Ebeling, H., & Sun, M. 2014, MNRAS, 443, L114
Schlafly, E. F., & Finkbeiner, D. P. 2011, ApJ, 737, 103
Smith, R. J., Lucey, J. R., Hammer, D., et al. 2010, MNRAS, 408, 1417
Storey, P. J., & Zeippen, C. J. 2000, MNRAS, 312, 813
STScI Development Team 2020, stsynphot: synphot for HST and JWST, Astrophysics Source Code Library, ascl:2010.003
Tan, B., Oh, S. P., & Gronke, M. 2023, MNRAS, 520, 2571
The Astropy Collaboration 2018, AJ, 156, 123
Tomičić, N., Vulcani, B., Poggianti, B. M., et al. 2021a, ApJ, 907, 22
Tomičić, N., Vulcani, B., Poggianti, B. M., et al. 2021b, ApJ, 922, 131
Tonnesen, S., & Bryan, G. L. 2012, MNRAS, 422, 1609
van der Walt, S., Schönberger, J., Nunez-Iglesias, J., et al. 2014, PeerJ, 2, e453
Vulcani, B., Fritz, J., Poggianti, B. M., et al. 2020a, ApJ, 892, 146
Vulcani, B., Poggianti, B. M., Gullieuszik, M., et al. 2018, ApJL, 866, L25
Vulcani, B., Poggianti, B. M., Tonnesen, S., et al. 2020b, ApJ, 899, 98
Werle, A., Poggianti, B., Moretti, A., et al. 2022, ApJ, 930, 43
Wisnioski, E., Glazebrook, K., Blake, C., et al. 2012, MNRAS, 422, 3339
Zanella, A., Le Floc'h, E., Harrison, C. M., et al. 2019, MNRAS, 489, 2792